ChemPubSoc Europe

DOI: 10.1002/ejic.201801394

EurJIC European Journal of Inorganic Chemistry

Full Paper

Mineral Ore Processing

Iron Carbonate Beneficiation Through Reductive Calcination – Parameter Optimization to Maximize Methane Formation

Susanne Lux,*[a] Georg Baldauf-Sommerbauer,[a] Bernhard Ottitsch,[a] Astrid Loder,[a] and Matthäus Siebenhofer[a]

Abstract: Direct iron carbonate reduction through reductive calcination in a hydrogen atmosphere is a high-potential candidate for environmentally benign pig iron production. In addition to the direct formation of elemental iron in one reaction step, carbon dioxide is only partially released from the carbonate. Instead, carbon monoxide, methane, and higher hydrocarbons form as gaseous reaction products. The experimental study described here is based on Mg-Mn substituted iron carbonate ore. First, the chemical thermodynamics of the reductive calcination of iron, magnesium, and manganese carbonate are discussed. The influence of temperature and pressure on equilibrium conversion is reviewed together with the accessible products. Results for the reductive calcination of mineral iron carbonate in a tubular reactor setup are presented. The methane yield was optimized via statistically planned design of experiments. The gauge pressure and temperature showed a statistically significant effect on the total iron carbonate conversion, as well as on carbon monoxide, and methane yield.

Introduction

Mitigation of carbon dioxide emissions (CO_2) is a predominant topic in current chemical engineering research. Direct process CO_2 emissions, as encountered in the beneficiation of mineral carbonates, need to be addressed by either process optimization, introduction of novel process concepts, and/or carbon dioxide utilization approaches.

Within the industrial sector, which is responsible for approximately one-third of the total anthropogenic CO_2-equivalent emissions, iron and steelmaking adopt leading roles, accounting for 13–25 % of emissions.[1,2] The global steel production and demand is steadily increasing (1.53 Gt in 2013 to 1.60 Gt in 2015)[3] and is not expected to decrease within this century. Even with the increasing share of recycled steel (= secondary steel),[4,5] primary production from iron ores will continue to be a major contributor to steel production and, thus, CO_2 emissions. In regions with major mineral iron carbonate (= siderite) reserves, such as China[6] and Austria,[7] iron and steel production is based on siderite ores. Due to the lower iron content of siderite compared to magnetite (Fe_3O_4) and hematite (Fe_2O_3) ores, its beneficiation poses a challenge. The industrial practice includes blending siderite with other high-grade ores in a sinter plant where it is converted to hematite by roasting it in the presence of air and subsequently feeding the sinter product to the blast furnace for reduction with coal via CO.[8,9] This conventional route releases at least 2.5 mol of CO_2 during the production of one mol of iron from iron carbonate due to the stoichiometry of the reaction.

As an alternative to state-of-the-art beneficiation of mineral iron carbonate, reductive calcination was introduced recently and applied as a means of carbon dioxide utilization during mineral carbonate beneficiation.[10,11] Instead of simply releasing CO_2 into the atmosphere, reduced carbon species such as carbon monoxide (CO), methane (CH_4) or even higher hydrocarbons are obtained, thus, adding value to the off-gas.

The term *reductive calcination* describes the conversion of a metal carbonate ($MeCO_3$) into a metal oxide (MeO) or elemental metal (Me) via calcination in a hydrogen atmosphere (= hydrogenation, Equation 1). Thus, this process involves a combination of carbonate calcination (Equation 2) and/or carbonate reduction (Equation 3) with carbon dioxide hydrogenation (Equation 4). We solely consider the formation of products containing one carbon atom (= C_1 products) in this publication, even though the formation of higher hydrocarbons has been mentioned in the literature.[12,13] However, the formation of > C_1 products was not observed in this study. Members of the scientific community disagree about the mechanism of formation of reduced carbon species in the gas. While some researchers have proposed the preceding release of CO_2 from the carbonate and its subsequent reduction with hydrogen on catalytically active sites, others have assumed that direct formation takes place on the solid surface. Reductive calcination is applicable to any carbonate within thermodynamic feasibility. In this work, the focus was placed on iron carbonate and on magnesium and

[a] *Graz University of Technology, Institute of Chemical Engineering and Environmental Technology, NAWI Graz, Inffeldgasse 25C/II, 8010 Graz, Austria*
E-mail: susanne.lux@tugraz.at
https://www.tugraz.at/institute/ceet/home/

Supporting information and ORCID(s) from the author(s) for this article are available on the WWW under https://doi.org/10.1002/ejic.201801394.

manganese carbonate accompanying iron carbonate in mineral iron carbonate (Me = Fe, Mg, Mn).

$$(a+b)\ MeCO_3(s) + [(a+b)\ (c/2+d) + b]\ H_2(g) \rightarrow a\ MeO(s) + b\ Me(s) + (a+b)\ CHcO_{2-d}(g) + [b+d\ (a+b)]\ H_2O(g) \quad (1)$$

$$a\ MeCO_3(s) \rightarrow a\ MeO(s) + a\ CO_2(g) \quad (2)$$

$$b\ MeCO_3(s) + b\ H_2(g) \rightarrow b\ Me(s) + b\ CO_2(g) + b\ H_2O(g) \quad (3)$$

$$CO_2(g) + (c/2 + d)\ H_2(g) \rightarrow CH_cO_{2-d}(g) + d\ H_2O(g) \quad (4)$$

Salotti and Giardini were the first authors to describe the hydrogenation of siderite.[12] They investigated the effect of temperature (345–605 °C) and initial hydrogen pressure (1.4–34 MPa H_2) on product formation. As solid products, elemental Fe and wuestite (FeO) were formed at temperatures above 455 °C, while at lower temperature, magnetite was obtained. As ubiquitous gaseous products, CH_4 and H_2O were derived. CO, CO_2, and the higher hydrocarbons ethane (C_2H_6), propane (C_3H_6), and butane (C_4H_{10}) formed in minor amounts over a limited temperature and pressure range. Salotti and Giardini postulated that a reaction took place directly on the mineral surface, yielding hydrocarbons rather than releasing CO_2 and subsequently reacting with hydrogen.

Emmenegger confirmed the formation of mainly elemental Fe together with FeO for siderite hydrogenation in an atmosphere of pure hydrogen.[14] As gaseous products, CH_4, H_2O, CO, and released CO_2 were mentioned. Higher hydrocarbons did not form. Emmenegger and Reller et al. dedicated the formation of CO and CH_4 to the reduction of released CO_2 on in situ formed catalytically active transition-metal species.[15]

In a previous publication, we suggested the hydrogenation of mineral iron carbonate as a means to achieve sustainable iron production.[10] The approach taken to reduce $FeCO_3$ directly with hydrogen to elemental iron avoids the formation of Fe_2O_3. Consequently, the CO_2 emissions decrease by 60 %, and up to 33 % less reducing agent is needed for iron production. Thermogravimetry was applied to determine the kinetics of the iron formation from siderite, including the concomitant decomposition of the accessory matrix of calcium, magnesium, and manganese carbonate. The formation of CO, CH_4, and higher hydrocarbons was not considered. The purpose of this paper is to foster the concept of reductive calcination. Based on the results of thermogravimetric experiments, reductive calcination in hydrogen is compared to calcination in an inert nitrogen atmosphere. The results of the product characterization of previous thermogravimetric studies[10,16] are supplemented with further findings. However, for complete exploitation of the benefits of reductive calcination, further attention needs to be turned to the gaseous reaction products. Thus, the main focus of this work was placed on methane formation during hydrogenation of siderite. The experiments were statistically planned based on design of experiments (DoE) to maximize the methane yield. The investigations were based on iron carbonate mineral (ICM) with Mg-Mn-substituted siderite as the main iron-containing phase and a siderite-enriched phase (SEM). These were performed in a thermobalance and a tubular reactor setup. The transferability of the thermogravimetric (TG) results to the tubular reactor (TR) results is also discussed.

Chemical Thermodynamics of Reductive Calcination

Influence of Temperature on the Equilibrium Composition

As the iron carbonate ore investigated in this study consists of Mg-Mn-substituted siderite as the main iron-containing phase, the chemical thermodynamics of iron, magnesium, and manganese carbonate are discussed in the following section.

The standard free energies of the reaction $\Delta_R G°$ for the formation of the bivalent iron oxide FeO and the mixed bi/trivalent oxide Fe_3O_4 lie in a comparable range.[16] The formation of FeO and Fe_3O_4 is favored over the formation of Fe_2O_3. For more details, refer to ref.[16] Magnesium carbonate is not known to form stable oxides other than the bivalent MgO. Furthermore, the reduction of $MgCO_3$ with hydrogen to form elemental magnesium according to Equation 3 is thermodynamically not feasible below 2000 °C and neither is the reduction of manganese carbonate to elemental manganese. The formation of elemental iron is feasible from a thermodynamic point of view, whereas iron oxide formation is slightly favored over iron formation. Due to the difference in $\Delta_R G°$, the calcination temperature can be expected to be 200–300 °C higher for magnesium carbonate and manganese carbonate as compared to iron carbonate (Figure 1). Moreover, formation of bivalent oxides from $FeCO_3$ and $MnCO_3$ is more complex compared to $MgCO_3$.

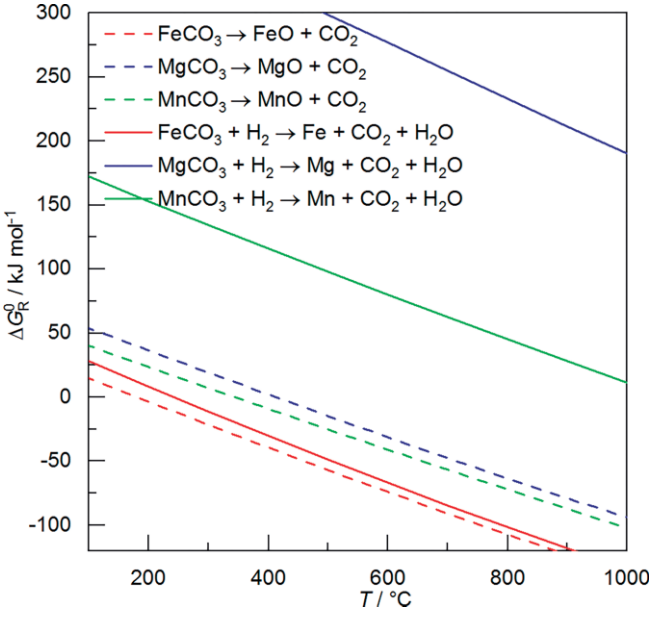

Figure 1. Standard free energy of reaction $\Delta_R G°$ for the conversion of iron, magnesium, and manganese carbonate into bivalent oxides and elements at ambient pressure. Calculations were performed with HSC Chemistry 8.0.6, assuming the formation of gaseous CO_2 and H_2O.

The general Equation 4 for the hydrogenation of carbon dioxide to C_1 products can be applied to represent the formation of carbon monoxide (CO, Equation 5), formic acid (HCOOH, Equation 6), formaldehyde (HCHO, Equation 7), methanol (H_3COH, Equation 8), and methane (CH_4, Equation 9).

$$CO_2(g) + H_2(g) \rightarrow CO(g) + H_2O(g) \quad (5)$$

$CO_2(g) + H_2(g) \rightarrow HCOOH(g)$ (6)

$CO_2(g) + 2\ H_2(g) \rightarrow HCHO(g) + H_2O(g)$ (7)

$CO_2(g) + 3\ H_2(g) \rightarrow H_3COH(g) + H_2O(g)$ (8)

$CO_2(g) + 4\ H_2(g) \rightarrow CH_4(g) + 2\ H_2O(g)$ (9)

The temperature dependency of $\Delta_R G°$ for the hydrogenation reactions (Equations 5–9) is approximately linear in the temperature range T = 0–1000 °C at ambient pressure (Figure 2, for linear fit data, see Supporting Information Table S-1). In the case of CO formation [Equation 5, also referred to as the reverse water-gas-shift (RWGS) reaction], $\Delta_R G°$ decreases with temperature, whereas $\Delta_R G°$ increases for all other reactions (Equations 6–9). The formation of formic acid and formaldehyde is thermodynamically not favorable, as $\Delta_R G°$ is above +40 kJ mol^{-1} at 0 °C and increases with temperature. Methanol formation could proceed at low temperatures (< 150 °C) as $\Delta_R G°$ is ≈ 0 at 0 °C, but it shows a strong increase with temperature [$d(\Delta_R G°)/dT$ = 0.2 kJ mol^{-1} °C^{-1}]. Methane formation is highly favorable below 450 °C ($\Delta_R G°_{450\ °C}$ = −30 kJ mol^{-1}) and shows a gradient of $d(\Delta_R G°)/dT$ = 0.2 kJ mol^{-1} °C^{-1}, which is comparable to that of methanol formation. Carbon monoxide formation can be expected in the whole temperature range evaluated (0–1000 °C) as $\Delta_R G°$ decreases, with a low gradient of $d(\Delta_R G°)/dT$ = −0.04 kJ mol^{-1} °C^{-1} compared to those of the other products (HCOOH, HCHO, H_3COH, CH_4) from approximately +30 kJ mol^{-1} at 0 °C to approximately −5 kJ mol^{-1} at 1000 °C.

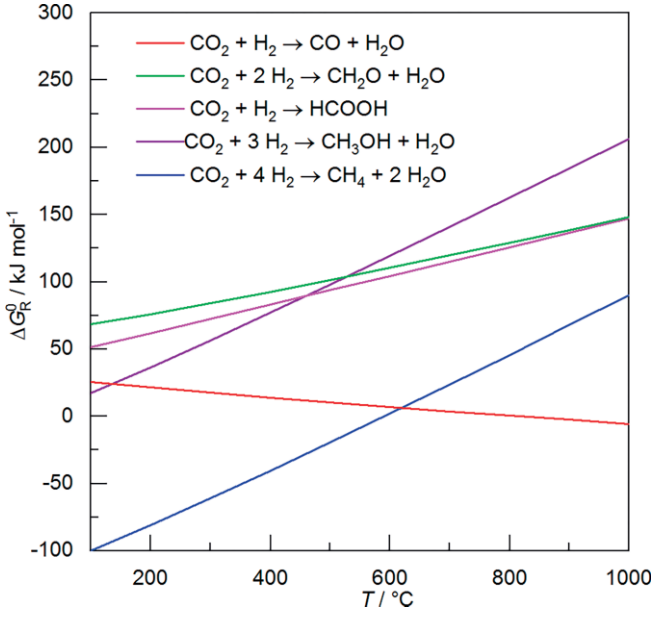

Figure 2. Standard free energy of reaction $\Delta_R G°$ for the hydrogenation of carbon dioxide to produce carbon monoxide (red), formic acid (magenta), formaldehyde (green), methanol (violet), and methane (blue) at ambient pressure. Calculations were performed with HSC Chemistry 8.0.6, assuming gaseous compounds.

Influence of Pressure on the Equilibrium Composition

The initial influence of an increase in pressure in a closed reaction system can be evaluated by applying Le Chatelier's principle, which assumes ideal gas behavior. A stoichiometric equation can be generalized, as expressed in Equation 10 for i compounds I with the respective stoichiometric coefficient $\in_j$. The stoichiometric coefficient is positive for products and negative for reactants.

$$\sum_i \epsilon_i I = 0 \quad (10)$$

with ϵ_i…stoichiometric coefficient for compound I

As a first approximation, volume changes can be neglected for liquid and solid reactants and products. Therefore, the change in the reaction volume in a closed system only depends on the change in the gaseous reactants. A positive change in gaseous reactants [$\Sigma_i \in_i$(gaseous) > 0] would lead to a volume increase, a negative change in gaseous reactants [$\Sigma_i \in_i$(gaseous) < 0] would lead to a volume decrease. In a closed system, Le Chatelier's principle states that the equilibrium product yield would decrease for $\Sigma_i \in_i$(gaseous) > 0 and the equilibrium yield would increase for $\Sigma_i \in_i$(gaseous) < 0 when the pressure is increased.

Consequently, an increase of pressure negatively affects calcination (Equation 2) and metal formation via reduction with hydrogen (Equation 3), as $\Sigma_i \in_i$(gaseous) = 0 for Equations 2 and 3 if H_2O is considered to be gaseous. According to Equation 5, carbon monoxide formation is not affected by an increase in pressure, as $\Sigma_i \in_i$(gaseous) = 0. The equilibrium yield of formic acid (Equation 6), formaldehyde (Equation 7), methanol (Equation 8), and methane (Equation 9) can be expected to be increased by pressure, as $\Sigma_i \in_i$(gaseous) = −1 if H_2O is considered to be gaseous and expected to be even lower if H_2O is partially condensed.

DoE for Statistically Planned Parameter Optimization of Methane Yield

The concept of Design of Experiments (DoE) was applied to plan parameter optimization with the aim of increasing the methane yield in the gas stream. A two-level fractional factorial 2^{6-1} design for six factors was used. The factors were: A = gauge pressure, B = temperature, C = amount of solid, D = H_2/N_2 feed ratio, E = feed flow rate, and F = size range. The two levels (+/−) for each factor are shown in Table 1.

Table 1. Experimental parameters (= factors) that were varied (−/+ level) in the steady state reductive calcination of the iron carbonate mineral in a study planned by design of experiments.

Factor	Dimension	−	+
A = Gauge pressure	bar	0	8
B = Temperature	°C	350	375
C = Amount of solid	g	60	104
D = H_2/N_2 feed ratio	–	60:40	90:10
E = Feed flow rate	cm^3_{STP} min^{-1}	500	867
F = Size range	mm	0.5–1.0	5–10

Factors A through F were varied under otherwise constant experimental conditions, and the effect on mass loss of the solid product (= a measure for the total conversion), CO, and CH_4 yield was evaluated statistically. The statistical evaluation was performed according to the methodology introduced by

Lenth[17] and applied i.a. by Frontistis et al.[18] A fractional design with the generator ABCDE = F was chosen to decrease the number of experiments compared to a full factorial design. A full factorial design for six factors includes 64 experiments, whereas a 2^{6-1} fractional design includes 32 experiments. This design was chosen because of the high information output – no main effects or two-effect interactions are aliased[19] – while the necessary experimental time is cut by half. The Lenth Pseudo-Standard-Error PSE was calculated as described in ref.[17]

The value of the reference line f_{ref} (also referred to as margin of error) in the bar plots (Figure 9 to Figure 11) was calculated from the PSE, and the value $t_{0.95,d}$ 2.22 (for d = 31) was calculated for a 95 % confidence interval of a standard Student's t-distribution according to Equation 11.

$$f_{ref} = PSE \cdot t_{0.95,d} \quad (11)$$

with f_{ref}... value of the reference line (margin of error), PSE... Lenth Pseudo-Standard-Error, t...t value for a 95% confidence interval of a standard Student's t-distribution

Results and Discussion

Product Characterization and Proposed Reaction Mechanism for Reductive Calcination in H_2 vs. Calcination in N_2

All liquid samples of tubular reactor experiments collected in vessels 1 and 2 were color- and odorless. The TOC was below 1000 ppm in all cases. According to the reaction equations, water is the only condensable non-carbonaceous compound that forms during reductive calcination (Equation 1) at 0 °C. Therefore, we concluded that the liquids collected in vessels 1 and 2 consisted of > 99 %wt. H_2O.

Figure 3 shows the thermogravimetric curves for the results of five linear heating rate experiments (3 °C min^{-1}) with 2 g of ICM and SEP (100–200 μm) in nitrogen and hydrogen atmosphere. The solid products of these experiments were analyzed by XRD (Figure 4, Table S-2 in Supporting Information) and ICP-OES (Table S-3 in Supporting Information). As already pointed out in ref.,[16] calcination in a nitrogen atmosphere led to the formation of wuestite and magnetite (both with Mg and Mn substitution) from the Mg-Mn siderite. The calcium-iron oxide srebrodoloskite $Ca_2Fe_2O_5$ (with Mg and Mn substitution) was produced from ankerite (Figure 4). When the ICM is heated at 3 °C min^{-1} to 640 °C and immediately cooled to 300 °C at a rate of approximately –11.4 °C min^{-1} (see black lines in Figure 3 and Figure 4) ankerite was present along with Mg-Mn-substituted wuestite and magnetite, whereas srebrodoloskite was formed in traces only. This means that ankerite was only partially converted below 640 °C, and a low conversion of ankerite was expected during calcination in nitrogen at lower temperatures.

Reductive calcination with an inlet flow of 70 %vol. H_2 led to a shift in the thermogravimetric curves of 40–50 °C compared to the curves observed with a pure N_2 inlet flow (Figure 3). This is explained by the higher thermal conductivity and heat capacity of H_2 compared to N_2 and the chemical interaction of H_2 with the solid reactant. The reaction temperature is decreased in reductive calcination compared to calcination in nitrogen, and the mass loss is increased. This mass is dedicated to the formation of iron instead of iron oxides. Iron formation can be described with a single step A2 reaction for SEP.[10] In the case of ICM, two clearly separable steps can be detected in the thermogravimetric curve. Although iron is present in ICM in siderite and, after reductive calcination at a maximum temperature of 740 °C, ankerite, iron is formed as one phase, and the accompanying elements are present in separate, oxidic phases.

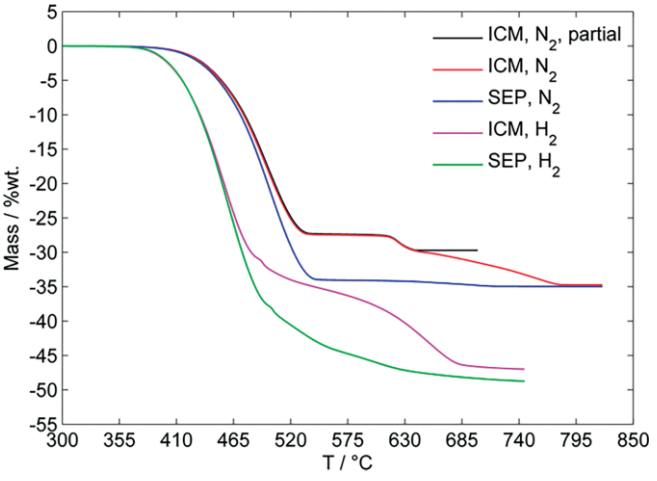

Figure 3. Thermogravimetric curves for the calcination of the iron carbonate mineral (ICM) and the siderite enriched phase (SEP) in nitrogen (black, red, blue) and 70 %vol. hydrogen (magenta, green). All samples were heated at a linear rate of 3 °C min^{-1} to either 640 °C (ICM, N_2, partial), 745 °C (ICM and SEP, H_2), or 825 °C (ICM and SEP, N_2). Initial weight = 2 g, 100 cm^3_{STP} min^{-1} total inlet flow rate, N_2: 100 %vol. nitrogen at the inlet, H_2: 70 %vol. hydrogen + 30 %vol. nitrogen at the inlet.

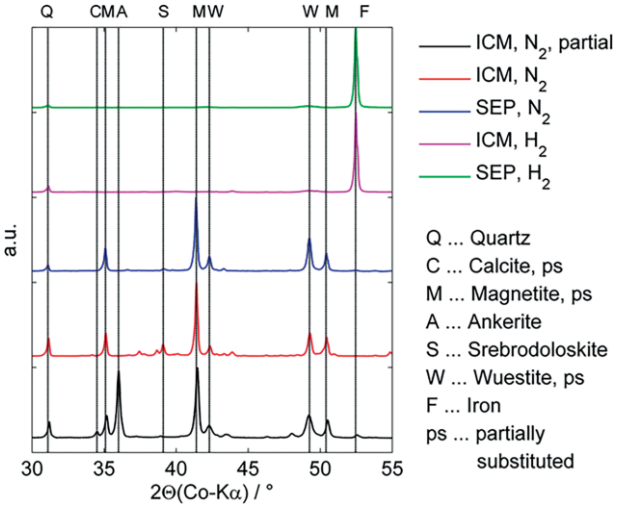

Figure 4. XRD pattern in the 30–55° range of the products of the thermogravimetric experiments presented in Figure 3. "Partially substituted" means that the main element (e.g., iron in wuestite FeO) can be partially substituted by magnesium or manganese.

The results of the elemental analysis (Supporting Information, Table S-3) agreed with the results of the XRD analysis. As expected, the iron content of the product of reductive calcination was increased compared to the product of calcination in nitrogen due to the formation of iron instead of iron oxides. Taking the results of the XRD analysis into account, the formal composition of the reaction products could be calculated from the elemental analysis (Table 2). A consistent result was generated, as summation of the proposed solid products is in the range of 100 ± 2 %wt.

Table 2. Composition of the solid products of the thermogravimetric calcination of a 100–200 μm fraction of ICM and SEP in nitrogen (columns 2 and 3) and 70 %vol. hydrogen (columns 4 and 5), calculated from the results of ICP-OES analysis.[a]

	ICM, N_2	SEP, N_2	ICM, H_2	SEP, H_2
Fe, %wt.	0	0	64.6	79.0
FeO, %wt.^{RIR}	30.5	32.6	0	0
Fe_3O_4, %wt.^{RIR}	39.9	51.0	0	0
MgO, %wt.	6.17	5.19	7.25	6.57
MnO, %wt.	4.17	4.65	4.87	5.67
CaO, %wt.	8.61	2.27	9.37	2.74
SiO_2, %wt.	7.81	4.00	9.00	4.73
Al_2O_3, %wt.	2.87	2.46	3.17	2.87
Sum, %wt.	100	102	98	102

[a] RIR: The phase ratio determined via RIR analysis of the XRD pattern was used to distinguish FeO and Fe_3O_4.

Transferability of Thermogravimetric Experiments to Calcination in a Tubular Reactor

The transferability of the results from thermogravimetric experiments to the results of calcination performed in the tubular reactor are discussed on the basis of five tubular reactor experiments Exp1–Exp5 (Figure 5).

The general experimental procedure is described in point a) of the experimental section, and the operation conditions were as follows:

Exp1. ICM was calcined in 100 %vol. nitrogen feed with a final temperature of 500 °C.

Exp2. ICM was calcined at a maximum temperature of 500 °C with a feed of H_2/N_2 = 9:1 until the product gas concentration of CO_2 fell below 0.2 %vol.

Exp3. Experiment Exp2 was repeated with an additional final holding time of 2 hours.

Exp4. Day1 = repetition of experiment Exp2; Day2 = reduction of the solid product of Day1 with a feed of H_2/N_2 = 6:4 at 400 °C for 5 hours.

Exp5. Day1 = repetition of experiment Exp2; Day2 = oxidation of the solid product of Day1 with a feed of CO_2/N_2 = 1:4 at 400 °C for 5 hours.

Hg-porosity measurements were performed with the iron carbonate mineral and the solid products of Exp1–Exp3. The ICM did not reveal any porosity. During calcination in N_2 (Exp1) and reductive calcination (Exp2, Exp3), a porous solid formed due to the release of carbon dioxide from the solid. The specific surface area varied between 5 and 7 $m^2\ g^{-1}$, whereas the porosity was higher for the products of reductive calcination (42–47 %) compared to the product of calcination in nitrogen (27 %, Table 3). The pore size distribution was relatively narrow for all products (Supporting Information, Figure S-1). The average pore diameter was lower for the product of calcination in N_2 (72 nm) compared to the products of reductive calcination (128–155 nm). For reductive calcination, the average pore diameters were 128 nm for short experiments and 155 nm for long experiments, whereas the specific surface areas were 7.2 and 5.3 $m^2\ g^{-1}$ for short and long experiments, respectively. Higher pore diameters but smaller specific surface areas at longer reaction times could result from a decreasing number of larger pores with increasing time of reaction.

Comparable XRD results were obtained with the 2–5 mm size fraction of the ICM calcined in the tubular reactor and the 100–200 μm-sized fraction investigated in the thermogravimetric experiments (Table 4 and Figure 6). Calcination in nitrogen led to the formation of a mixture of wuestite and magnetite. Ankerite was not decomposed in the tubular reactor experiments, as the reaction temperature was limited to 500 °C. This finding is reasonable with respect to the thermogravimetric results. Reductive calcination at 500 °C, conducted until the product gas composition decreased to 0.2 %vol. CO_2 (= Exp2), led to the formation of wuestite, iron, and magnetite, whereas the wuestite to magnetite ratio was increased compared to the ratio observed with calcination in nitrogen. When the reductive calcination was performed for two more hours in a single experiment (Exp3), the iron content increased, the wuestite level decreased, and magnetite was not present due to reduction of the oxides with hydrogen. Exp2 was repeated, and the reduction with hydrogen was performed for five hours at 400 °C in a different experiment, leading to the confirmation of iron formation from the iron oxides produced in Exp2. The lower iron content of the product of Exp3 compared to Exp4 can be explained by the fact that a lower reaction temperature was applied in Exp4 (400 °C) compared to Exp3 (500 °C). When Exp2 was repeated and the solid product was treated with a feed gas containing 20 %vol. CO_2 in a follow-up experiment (=Exp5), the wuestite and iron levels decreased and magnetite levels increased due to the oxidation of iron and wuestite with CO_2 (Equation 12). The mass loss observed for the ICM after Exp1–Exp3 coincides with the XRD results. The mass loss was higher for short reductive calcination (31.92 %wt. for Exp2) compared to calcination in N_2 (27.98 %wt. for Exp1) due to the higher amount of wuestite and iron formed in the reductive calcination process as compared to the calcination process in N_2 (see Supporting Information, Table S-4). The mass loss decreased further, 35.16 %wt. for Exp3 compared to 31.92 %wt. for Exp2, when the reaction time for reductive calcination was extended. This can be explained by the increase in iron and decrease in wuestite and magnetite content that occurred due to their reduction with H_2.

As pointed out earlier, the formation of methanol, formic acid, and formaldehyde was not expected at the reaction temperatures of 400–500 °C which were applied in the tubular reactor experiments Exp1–Exp5. This expectation was confirmed, as only CO, CO_2, and CH_4 were detected in the product gas, and the TOC value of the condensed liquids remained well below

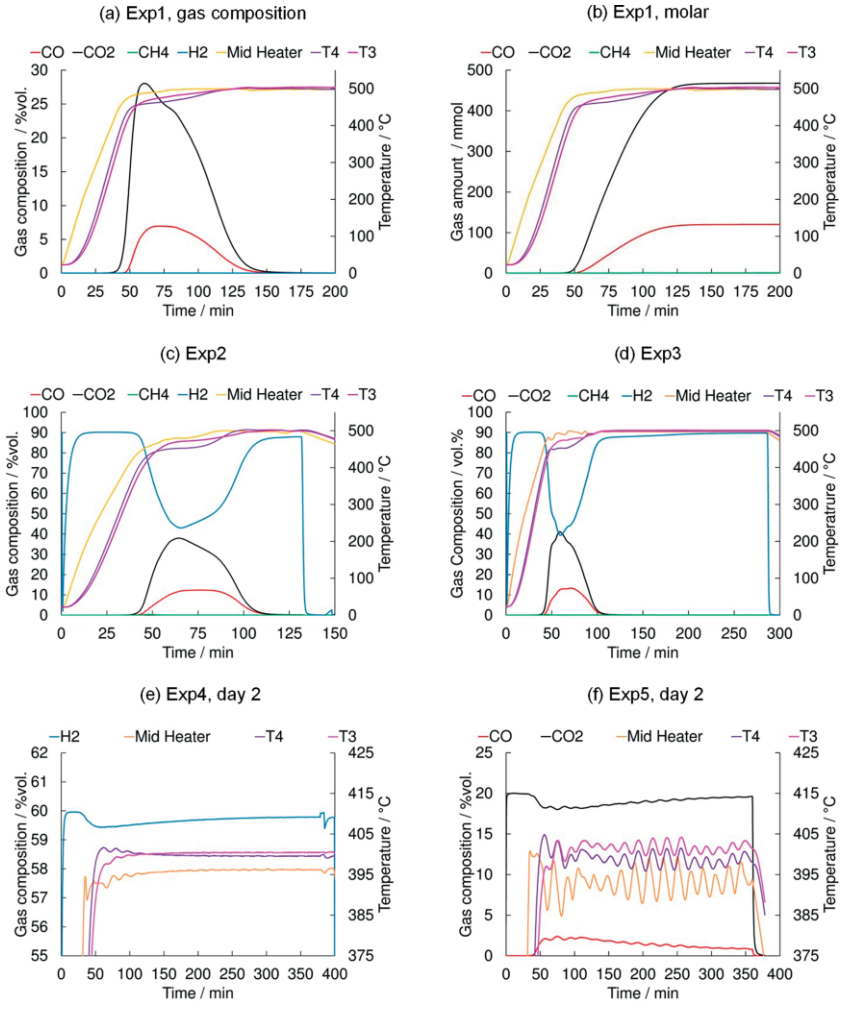

Figure 5. Tubular reactor experiments Exp1–Exp5. Gas composition data (CO/red, CO_2/black, CH_4/green, H_2/blue) refer to the left ordinate, temperature data (mid heater/orange, T4/purple, T3/magenta) to the right ordinate.

Table 3. Results of the porosity measurements of the solid products in Exp1–Exp3.

Experiment	Porosity[a] %	Specific surface area[b] $m^2\ g^{-1}$	Av. pore diameter[b] nm
Exp1: Calcination in N_2	27.4	6.7	72
Exp2: Reductive calcination, short	46.8	7.2	128
Exp3: Reductive calcination, long	42.0	5.3	155

[a] Ratio of pore volume to total external volume of the sample. [b] Equations for the calculation procedure are given in ref.[20]

Table 4. Several experimental results for the tubular reactor experiments Exp1–Exp3.[a]

Parameter	Exp1 N_2	Exp2	Exp3
1: H_2O (exp) /g	0	4.14	6.32
2: H_2O (calc) /g	2.18	2.83	2.79
3: CO /mmol	120	154	151
4: CO_2 /mmol	468	443	435
5: CH_4 /mmol	0	1.4	1.8
6: CO + CO_2 + CH_4 /mmol	588	598	588
7: Mass loss / %wt.	27.98	31.92	35.16
8: Fe(ICM) / %wt.	33.23	34.09	32.96
9: $FeCO_3$ (ICM,calc) /mmol	619	635	614

[a] 1: Amount of condensed water; 2: amount of water calculated from produced amounts of CO and CH_4 ($m_{H2O,calc}$•MW_{H2O} = n_{CO} + 2•n_{CH4}); 3–6: amounts of CO, CO_2, and CH_4 produced in each experiment and the sum thereof; 7: mass loss of the ICM after the experiment; 8: iron content of the ICM before the experiment; 9: theoretical $FeCO_3$ content of the ICM before the experiment ($n_{FeCO3,ICM,calc}$ = $n_{Fe,ICM}$ = $m_{0,ICM}$•w_{Fe}/MW_{Fe}).

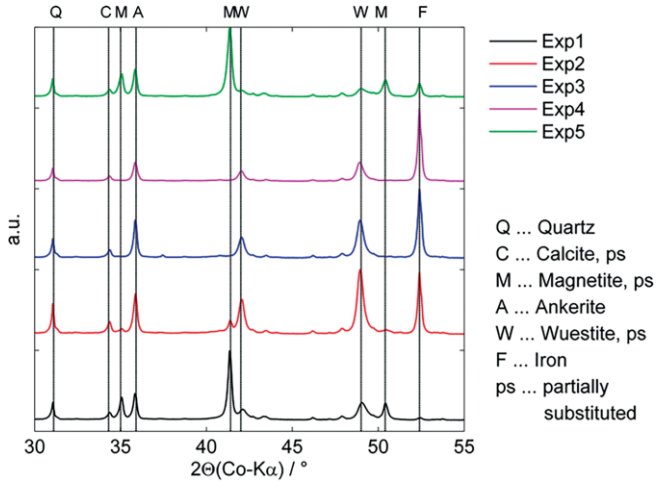

Figure 6. XRD pattern in the 30–55° range of the solid products of Exp1–Exp5.

1000 ppm. In Exp1–Exp3, CO_2 formation started in the heat-up phase, and CO formation was observed subsequently. CH_4 formation in trace amounts was observed during the heat-up phase of reductive calcination (Exp2 and Exp3) but not during calcination in N_2. The amount of released CO_2 reduced from 468 mmol in Exp1 to 435 mmol in Exp3 when the gas atmosphere was changed from inert to reducing (≈ 7 % CO_2 reduction). To further reduce CO_2 in the product gas and enhance methane formation, statistically planned design of experiments was perfiormed. Regardless of the calcining atmosphere (N_2 vs. H_2) both, the total amount of C_1 products formed ($CO + CO_2 + CH_4$ = 588–598 mmol) and the ratio of total C_1 products to the calculated $FeCO_3$ content of the ICM were within a comparable range (0.94–0.96). The CO formation can be explained by two reactions: wuestite oxidation (Equation 12) and RWGS (Equation 5). Calcination of the ICM in N_2 (Exp1) did not lead to the formation of water, and magnetite was detected in the solid product along with wuestite. Thus, the carbon monoxide produced can be attributed to the formation of magnetite via Equation 13.

$$FeO(s) + 1/3\ CO_2(g) \rightarrow 1/3\ Fe_3O_4(s) + 1/3\ CO(g) \quad (12)$$

An application of Equation 13 and Equation 14 allows for the calculation of the mass ratio of wuestite to magnetite $r_{WM,GA}$ from the molar ratio of CO and CO_2 τ_{MD} for calcination in N_2.

$$FeCO_3(s) \rightarrow (1\text{-}x)\ FeO(s) + x/3\ Fe_3O_4(s) + (1\text{-}x/3)\ CO_2(g) + x/3\ CO(g),\ x = 0\text{–}1 \quad (13)$$

$$\frac{m_{FeO}}{m_{Fe_3O_4}} = \frac{MW(FeO)}{MW(Fe_3O_4)} \cdot \frac{3 \cdot \left(1 - \frac{3\tau_{MD}}{1+\tau_{MD}}\right)}{\frac{3\tau_{MD}}{1+\tau_{MD}}}$$

with m... mass, MW... molecular weight, τ_{MD}... molar ratio of carbon monoxide and carbon dioxide (14)

The mass ratio of wuestite to magnetite was determined to be 0.485 based on the results of the XRD analysis and 0.589 based on the results of the gas analysis. These values are in a comparable range, and the increase in the magnetite content between the end of the experiment and after XRD analysis can be explained by the oxidation of magnetite that occurred in air during the sample preparation for XRD analysis (e.g., grinding, storage time). During the reductive calcination process (Exp2 and Exp3), on the contrary, water was formed. Carbon monoxide formation in a RWGS reaction (Equation 5) and methane formation (Equation 9) were coupled to the formation of water. The amount of water calculated from the amount of CO and CH_4 according to Equations 5 and 9, however, was lower than the amount of water produced during reductive calcination in Exp2 and Exp3. As evidenced by XRD, iron was formed in Exp2 and Exp3. This is a possible explanation for the increased water amount, as H_2O represents a hydrogen sink during reduction of iron oxides (Equation 15).

$$FeO_{1+x}(s) + (1 + x)\ H_2(g) \rightarrow Fe(s) + (1 + x)\ H_2O(g) \quad (15)$$

During thermogravimetric experiments, the mass change was measured online, whereas the product gas composition was measured online during tubular reactor experiments. Both signals were linked to the relative conversion via the general reaction equation (Equation 1). A balance of the C_1 products of tubular reactor experiments allowed for the calculation of the conversion of the carbonate into the oxide. Iron formation, however, was only detectable online during the thermogravimetric experiments from the mass loss. A hydrogen balance could be applied to account for iron formation during the tubular reactor experiments. The calculation of such a balance has some limitations, as it was derived on the basis of Exp3 in the Supporting Information. However, the results of the online-gas analysis of the tubular reactor experiments provides important information about the reaction mechanism. Firstly, the balance on CO, CO_2, and CH_4 provides a measure for the consumption of decomposable carbonates. As long as one of these compounds can be measured in the product gas, decomposable carbonates must be present in the ICM, which is fixed in the tubular reactor. Secondly, as long as the hydrogen content of the product gas remains below the content of the entering gas, hydrogen is consumed in either hydrogenation reactions (Equation 5–9) or in iron formation (Equation 1, Equation 15). During reductive calcination of the ICM in the tubular reactor (Exp2 and Exp3), most of the CO, CO_2, and CH_4 were produced 125 minutes after beginning of the heating phase. This finding is fortified by the hydrogen consumption observed in day 2 of Exp4 (Figure 5).

Based on these findings, the reaction mechanism depicted in Scheme 1 is proposed. Wuestite and carbon dioxide are the products of the thermal decomposition of the Mg-Mn siderite

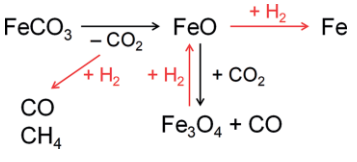

Scheme 1. Proposed reaction scheme for the reductive calcination of mineral iron carbonate. For purposes of clarity, the partial substitution of iron with magnesium and manganese in iron carbonate, wuestite, and magnetite is not depicted.

present in the ICM. Carbon dioxide produced during thermal decomposition can either undergo hydrogenation to CO and CH_4 or leads to the partial oxidation of wuestite to magnetite. Iron formation can be treated as a follow-up reaction. At first, wuestite and carbon dioxide are formed from iron carbonate. Subsequently, wuestite can either react with hydrogen to form iron or react with carbon dioxide to form magnetite.

Optimization of the Methane Yield Based on the Design of Experiments

Figure 7 demonstrates that the onset temperature for CO_2 formation in scanning experiments – and, thus, for carbonate decomposition and succeeding hydrogenation reactions in the gas phase – increases with the size range of the ICM. This can be explained by the transport limitations that occur as the particle diameter increases. Furthermore, the formation rate of carbon dioxide and monoxide $(dy_{COx})/dt = (dy_{COx})/dT \cdot dT/dt$ is higher than that of methane. The relative methane content of the product gas passed a peak at approximately 400 °C and decreased with increasing time and temperature (Figure 8). Several preliminary steady-state experiments conducted between 330 and 415 °C supported the assumption that was drawn from the results of the thermodynamic analysis: the CO yield increases with temperature, whereas the CH_4 yield decreases. However, in the preliminary experiments, only temperature was varied under otherwise constant conditions. Therefore, a statistically planned study on the influence of temperature, gauge pressure, size fraction, initial mass of the ICM, feed flow rate, and feed flow composition (see Table 1 for value of the factors) on mass loss of the solid sample, CO, and CH_4 yield was performed. The mass loss of the ICM due to calcination is a direct measure of the conversion of the solid. The use of a reference mass loss for a specific reaction product Δm_{ref} allows for the calculation of the conversion $X_{i-j,calc}$ of reactant ICM into a product containing wuestite and magnetite (Equation 16) with the experimental mass loss Δm_{exp}.

$$X_{ICM-WM,ml} = \frac{\Delta m_{exp}}{\Delta m_{ref}} \quad (16)$$

with X... conversion, Δm... mass loss

In the experiments, the reactor temperature was held at 530 °C for approximately one hour. After this hold time, practically no CO, CO_2, or CH_4 was detected in the product-gas for calcination in nitrogen. The average mass loss encountered in scanning experiments with a pure nitrogen feed was 27.5 %wt. This value can be interpreted as the maximum mass loss that corresponds with the complete conversion of the Mg-Mn siderite present in ICM into wuestite and magnetite $X_{ICM-WM,ml}$. Consequently, Equation 16 with Δm_{ref} = 27.5 %wt. was applied to quantify the conversion of the siderite fraction of the ICM into iron oxides after each experiment.

The main findings of the statistically planned study are shown in the bar plots in Figure 9, Figure 10, and Figure 11. The experimental results are summarized in Table S-6 in the Supporting Information. Negative effects are shown in red, and positive effects are shown in green. Every effect with an absolute value higher than the margin of error is statistically significant in a 95 % confidence interval of the Student's T-distribution. Thus, the gauge pressure and temperature showed a statistically significant effect on the total conversion $X_{ICM-WM,calc}$ (Figure 9). On average, the conversion was decreased by 20 % when the pressure was increased from an ambient pressure to 0.8 MPa gauge pressure. On the contrary, conversion was increased by 25 % when the temperature was increased from 350 to 375 °C. The carbon monoxide yield was primarily influenced by temperature and pressure (Figure 10). An increase in pressure led to an average 10 % decrease in the CO yield, whereas an increase in temperature led to an average 4 % increase in the CO yield. The methane yield was increased by pressure by 20 % and decreased by temperature by 13 % (Figure 11). The increase in the hydrogen in the feed positively affected the methane yield by 12 %. The initial amount of the ICM and feed flow rate showed opposing trends. A low amount of ICM and a high feed flow rate positively affected the methane yield by 6 %. The highest methane yield was achieved under conditions

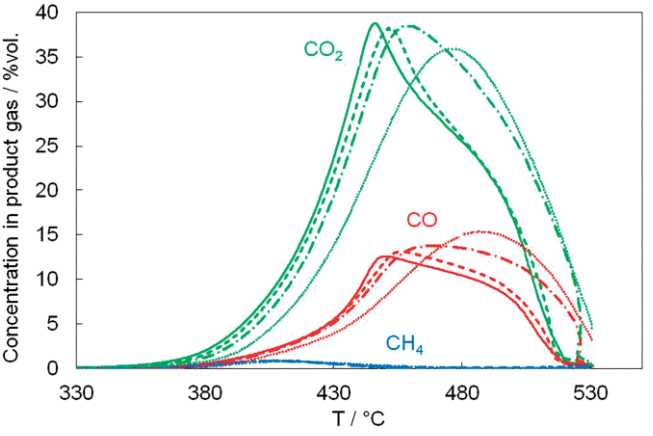

Figure 7. Scanning experiment with four size ranges [0.5–1 mm (–), 1–2 mm (- - -), 2–5 mm (-•-), and 5–10 mm (••••)] of the ICM in a feed flow of 500 cm^3_{STP} min^{-1} with a composition of H_2/N_2 = 9:1. Only the heat-up phase with a gradient of 1.5 °C min^{-1} is plotted; hence, the reaction time increased with temperature, red: CO, green CO_2, blue: CH_4.

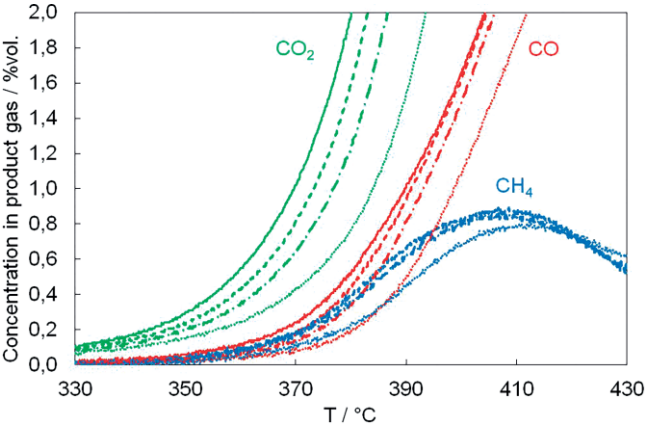

Figure 8. Close-up of one aspect of Figure 7 to demonstrate the range of CH_4 formation; scanning experiment with four size ranges [0.5–1 mm (–), 1–2 mm (- - -), 2–5 mm (-•-), and 5–10 mm (••••)] of the ICM in a feed flow of 500 cm^3_{STP} min^{-1} with a composition of H_2/N_2 = 9:1.

that could be predicted from the bar plot shown in Figure 11: high pressure (8 bar), low temperature (350 °C), low amount of ICM (60 g), high size range (5–10 mm), high amount of hydrogen in the feed (H_2/N_2 = 9:1), and high feed flow rate (867 cm^3_{STP} min^{-1}). Under the conditions specified, the selectivity for methane was 75 %.

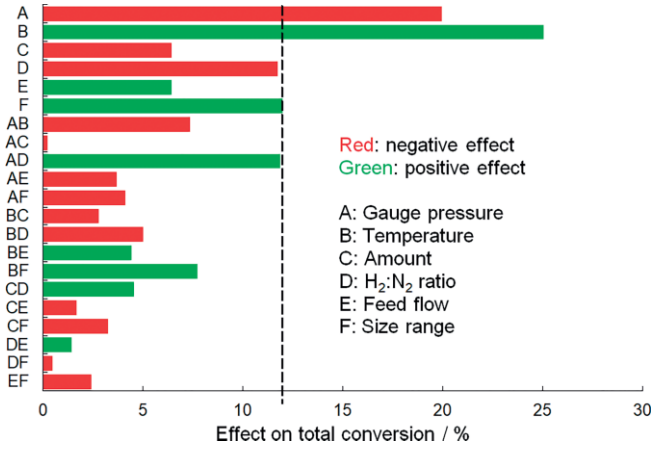

Figure 9. Effect of factors A–F on the total conversion of the ICM into iron oxides.

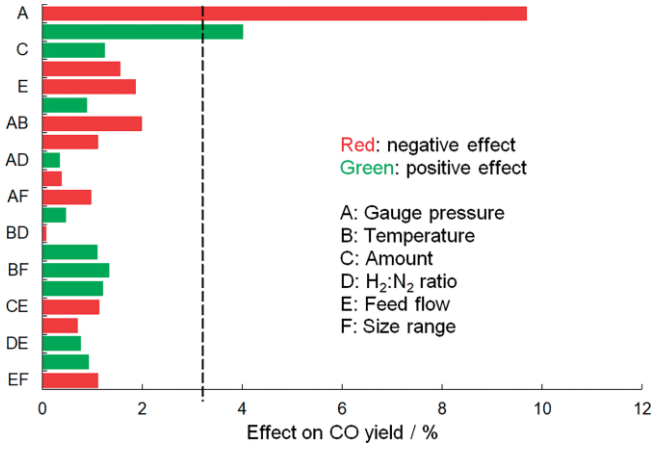

Figure 10. Effect of factors A–F on the carbon monoxide yield.

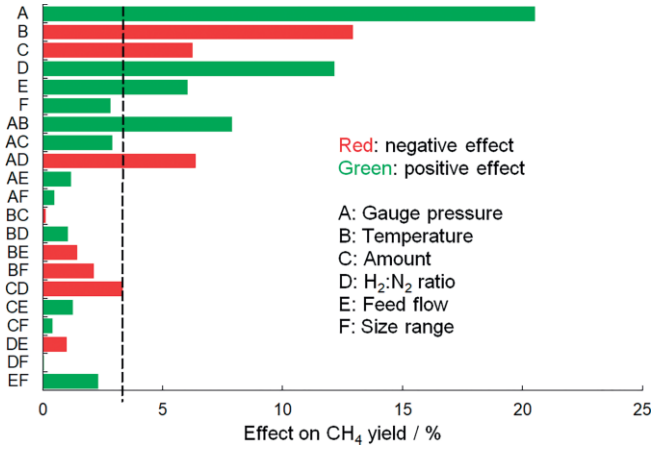

Figure 11. Effect of factors A–F on the methane yield.

Conclusions

The thermodynamic analysis of the reductive calcination of iron and magnesium carbonate revealed that the accessible products are FeO, Fe_3O_4, Fe, MgO, CO, CO_2, and CH_4 in the temperature range of 0–1000 °C. As expected, methane formation is favored at low temperature and increased pressure. This expectation was confirmed experimentally, and reaction conditions for increased methane yield were optimized via design of experiments, with the gauge pressure and temperature showing a statistically significant effect on total iron carbonate conversion.

When the pressure was increased from ambient pressure to 0.8 MPa gauge pressure, the conversion of iron carbonate decreased by 20 %. On the contrary, an increase of conversion by 25 % was achieved when the temperature was increased from 350 to 375 °C. Under the reaction conditions applied, iron carbonate conversion was up to 88 %.

For methane formation, the yield was increased by pressure by 20 % and decreased by temperature by 13 %. An increase of hydrogen in the feed positively affected the methane yield by 12 %. The selectivity for methane was 75 % at high pressure (8 bar), low temperature (350 °C), low amount of ICM (60 g), high size range (5–10 mm), high amount of hydrogen in the feed (H_2/N_2 = 9:1), and high feed flow rate (867 cm^3_{STP} min^{-1}).

In contrast, the formation of CO is favored at high temperature and low pressure. An increase in temperature led to an average 4 % increase in the CO yield, whereas an increase in pressure led to an average 10 % decrease in the CO yield.

This study highlighted the potential of reductive calcination for mineral iron carbonate beneficiation due to the formation of methane and carbon monoxide in the product gas instead of simply releasing carbon dioxide. It was shown that adjustment of the operation conditions during reductive calcination allows for a tailor-made product gas composition.

Experimental Section

Materials and Methods: The *i*ron *c*arbonate *m*ineral (ICM) from the Erzberg (Austria) was supplied by VA Erzberg GmbH in four size ranges: 0.5–1 mm, 1–2 mm, 2–5 mm, and 5–10 mm. A 100–200 µm fraction of the material and a *s*iderite *e*nriched *p*hase of the iron carbonate mineral (SEP; for preparation method see ref.[10]) were also used in previous studies.[10,16]

Wavelength dispersive X-ray fluorescence spectroscopy (XRF) was performed on a PW4400 Axios max (Panalytical) device. X-ray diffraction analysis (XRD) was performed on an X'Pert Pro (Panalytical) device using a cobalt radiation source ($K_{\alpha1}$ = 0.178901 nm, $K_{\alpha2}$ = 0.179290 nm) and the HighScore Plus software for phase detection and quantification by either the reference intensity ratio (RIR) or Rietveld refinement. Elemental analysis of solid samples was performed by means of ICP-OES (Spectro Acros, Spectro Ametek) and by chemical wet analysis (iron determination according to the procedure of Zimmermann–Reinhardt). The sample preparation method for ICP-OES analysis is described in ref.[21] The organic carbon content of liquid reaction products of tubular reactor experiments was analyzed by means of automated total organic carbon analysis (TOC-L-CPH, Shimadzu). Nitrogen and hydrogen of 99.999 %vol. grade and carbon dioxide of 99.998 %vol. grade were supplied by AirLiquide. An ABB AO2020 online gas analysis system

was used in tubular reactor experiments. Infrared absorption spectroscopy (ABB Uras26) was used to quantify the CO, CO_2, and CH_4 content (0.0–100.0 %vol.). A thermal conductivity module (ABB Caldos27) was used to quantify H_2 (0.0–100.0 %vol.). The online gas analyzer was frequently recalibrated with three different standard gas mixtures containing certified amounts of CO, CO_2, CH_4, H_2, and N_2 supplied by AirLiquide. Mercury porosity measurements were carried out on a Pascal 140/440 device provided by Thermo Finnigan with mercury in 99.9995 % quality (Roth) and a dry sample mass of ≈ 100 mg. Validation of the device and calculation procedures applied to the porosimetric results are described in ref.[20]

The composition of the 100–200 µm size fraction of the ICM used in the study presented in ref.[16] is quite comparable to the composition of the four size fractions (0.5–1, 1–2, 2–5, and 5–10 mm) used in the tubular reactor experiments discussed in this publication. Iron is the main constituent of the ICM (33.1–33.5 %wt.) and calcium, silicon, magnesium, and manganese are accompanying elements at a level of 2 to 4 %wt. Aluminum, sulfur, phosphorus, and potassium are present at levels below 0.5 %wt. For detailed information on the elemental composition, see Table S-2 in the Supporting Information. The variation of the metal content is small as verified by the small values of the absolute standard deviation. There is only a minor difference between the mean of each size range (e.g., w_{Fe} = 33.3 ± 0.2 % for size range 0.5–1 mm) and the mean of the size ranges 0.5–10 mm (e.g., w_{Fe} = 33.4 ± 0.2 % for all size ranges).

As all samples were taken from the same deposit and do show a comparable elemental distribution; therefore, the phase composition was not expected to vary significantly between samples and size ranges. As pointed out in ref.,[16] iron is present in two different carbonate phases: Mg-Mn-substituted siderite and ankerite, a Ca-Fe-Mg-Mn carbonate with the same crystal structure as dolomite.[22] Mg-Mn-substituted siderite is the main iron containing phase.[16] The iron content is distinctly higher in Mg-Mn siderite compared to in ankerite. It is challenging to determine the ratio of siderite to ankerite for each sample of the ICM used in reductive calcination experiments. The reflection signals of dolomite and ankerite overlap in the XRD pattern. Therefore, the quantification of phases via the reference intensity ratio (as applied in ref.[16]) or Rietveld refinement (as applied in this publication and ref.[20]) is challenging, as either dolomite or ankerite has to be used for quantification and the reflections can barely be distinguished. Iron, magnesium, and manganese are present in both siderite and ankerite; therefore, the elemental analysis cannot be used to distinguish phases. Decomposition steps encountered in thermogravimetric curves can give a hint about the phase ratio, as siderite decomposes at a lower temperature than ankerite. But also in the thermogravimetric approach, a stoichiometric formula for siderite and ankerite is needed to calculate the molar compositions.

Experimental Setup: In the course of this study, thermogravimetric experiments (TG) and experiments in a tubular reactor (TR) were performed. A Netzsch Jupiter STA 449C thermobalance and alumina sample beakers were used in all thermogravimetry experiments. For tubular reactor experiments, the setup delineated in Figure 12 was used. It was also used in previous studies described in refs.,[20,21,23] in which comparable sketches can be found. A detailed written description of the setup is given in ref.[21] A detailed sketch of the reactor tube and the thermocouple positioning can be found in ref.[20]

Experimental Procedures for Tubular Reactor Experiments: Stainless steel spacers were used to place the ICM bed inside the reactor tube. For the size fraction 0.5–1 mm, glass wool tori were employed above and below the solid bed to avoid the carry-over of the particles. The ICM bed forms a hollow cylinder inside the reactor tube. The bed height h_{ICM} can be estimated with Equation 17 from the mass m_{ICM}, the apparent density ρ_{ICM}, (≈ 1.69 g cm^{-3}, Table 5) the outer diameter of the thermocouple casing OD_{TC}, and the inner diameter of the reactor tube ID_{RT}.

$$h_{ICM,TR} = \frac{4}{\pi * (ID_{RT}^2 - OD_{TC}^2)} * \frac{m_{ICM}}{\rho_{ICM}} \quad (17)$$

with *h*... bed height, *m*... mass of the ICM bed, ID... inner diameter of the thermocouple chasing (TC), OD... outer diameter of the reactor tube (RT)

The feed composition of gas mixtures was adjusted with the gas analyzer. The feed gas flow was directed into the gas analyzer, bypassing the reactor tube and the set points of the mass flow controller (MFC) adjusted so that the desired feed gas composition was achieved under the prerequisite that the total flow was as defined. After setting up the desired inlet gas flow, the feed flow was di-

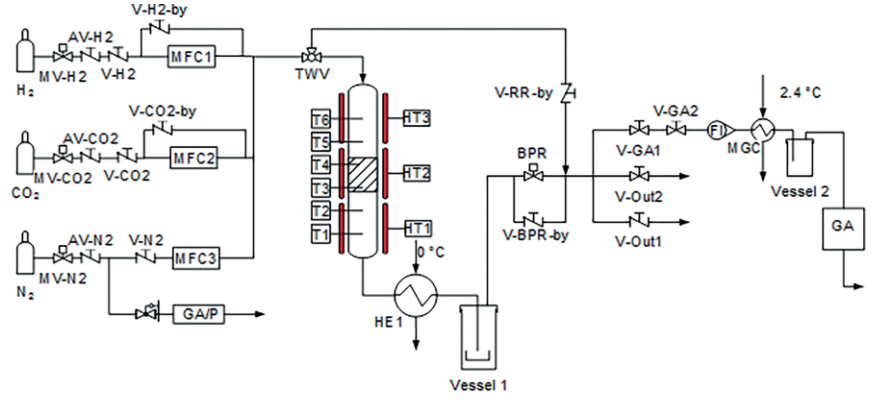

Figure 12. Sketch of the tubular reactor setup.

Table 5. Apparent densities of the four size fractions of the ICM.

Size fraction mm	Apparent density kg m^{-3}
0.5–1	1710
1–2	1690
2–5	1670
5–10	1670

rected into the reactor tube. This procedure was employed to overcome possible deviations of the MFC. The MFC could not be calibrated in-house, whereas the gas analyzer was checked and recalibrated frequently.

Several operation modes were employed for tubular reactor experiments:

a) Exp1–Exp5: 104 g of the ICM of the size fraction 2–5 mm were used, corresponding to a height of the ICM bed of 125 mm. The mean value of *T*3 and *T*4 was used as the target temperature T_{tar}, as this was the temperature nearest to the mid of the ICM bed. The feed flow rate was set to 500 cm^3_{STP} min^{-1}, and the feed gas composition was either 100 %vol. N_2 or H_2/N_2 = 9:1. The shut-off and weighing procedure was the same as for the scanning experiments. Liquid products collected in vessels 1 and 2 were saved for TOC analysis.

b) Scanning experiment – controlled increase of a target temperature T_{tar}: 115 g of the ICM were used, which corresponds to a bed of 147 mm for ρ_{ICM} = 1.685 g cm^{-3} (mean value of the size ranges). The feed flow rate was set to 500 cm^3_{STP} min^{-1}, and the feed gas was either pure N_2 or a mixture of hydrogen and nitrogen with a composition of H_2/N_2 = 9:1. Starting from room temperature and after an initial heating phase of 25–35 minutes, the heating power of all heating zones was adjusted manually, so that the average gradient of the target temperature T_{tar} was at 1.5 K min^{-1}. The mean value of *T*3 and *T*4 was used as T_{tar}, as this was the temperature nearest to the center of the ICM bed. When T_{tar} = 530 °C was reached, the reactor was operated at this target temperature for 1 hour before it was flushed with nitrogen and cooled to room temperature overnight. The next day, the solid product was filled into a polypropylene container under nitrogen flow and the output weight was determined immediately. Liquid products collected in vessels 1 and 2 were stored for TOC analysis.

c) Steady state reductive calcination for statistically planned (DoE) parameter study: 60/104 g of ICM were used, corresponding to a height of the ICM bed of 76/132 mm for size fraction 0.5–1 mm and 78/135 mm for size fraction 5–10 mm. The mean value of *T*3 and *T*4 was used as T_{tar}, as this was the temperature nearest to the mid of the ICM bed (see Supporting Information Figure S-2). The feed flow rate was set to 500/867 cm^3_{STP} min^{-1} and the feed gas composition was H_2/N_2 = 9:1/6:4. The reactor was heated to T_{tar} + 1 = 350/ 375 °C and operated for six hours at the target temperature. The shut-off and weighing procedure was the same as for the scanning experiments. Liquid products collected in vessels 1 and 2 were saved for TOC analysis.

Calculation of CO and CH_4 Selectivity: The procedure and equations applied to calculate the amount of carbon monoxide, carbon dioxide, and methane formed during experiments from the online gas analysis of the tubular reactor setup is described in ref.[21] The selectivity of carbon monoxide after time *t* ($S_{CO,t}$) was calculated with Equation 18, and the selectivity of methane after time *t* ($S_{CH4,t}$) was calculated with Equation 19 from the amounts $n_{i,t}$ of CO, CH_4, and CO_2 produced during the reaction.

$$S_{CO,t} = \frac{n_{CO,t}}{n_{CO2,t} + n_{CO,t} + n_{CH4,t}} \quad (18)$$

with *S*... selectivity, *n*... number of moles after time *t*

$$S_{CH4,t} = \frac{n_{CH4,t}}{n_{CO2,t} + n_{CO,t} + n_{CH4,t}} \quad (19)$$

with *S*... selectivity, *n*... number of moles after time *t*

Acknowledgments

The authors sincerely thank Herbert Schmid (voestalpine Stahl GmbH, Austria) and Alfred Stadtschnitzer and Armin Kogelbauer (VA Erzberg GmbH, Austria) for their valuable collaboration in the course of the project "RedK – Reduzierende Kalzinierung". The project was funded by the Austrian "Klima- und Energiefonds" in the framework of the program "Energy Mission Austria".

Keywords: Reductive calcination · Hydrogenation · Inorganic carbonate · Iron · Methane · Redox chemistry

[1] M. A. Quader, S. Ahmed, R. Ariffin, R. Ghazilla, S. Ahmed, M. Dahari, *Renewable Sustainable Energy Rev.* **2015**, *50*, 594–614.
[2] S. Pauliuk, R. L. Milford, D. B. Müller, J. M. Allwood, *Environ. Sci. Technol.* **2013**, *47*, 3448.
[3] W. S. Association, *Monthly Crude Steel Production* **2015** and 2016, **n.d**.
[4] M. Fischedick, J. Marzinkowski, P. Winzer, M. Weigel, *J. Cleaner Prod.* **2014**, *84*, 563–580.
[5] J. Fu, G. Tang, R. Zhao, W. Hwang, *J. Iron Steel Res. Int.* **2014**, *21*, 275–281.
[6] D. Zhu, X. Zhou, J. Pan, Y. Luo, *Miner. Process. Extr. Metall.* **2014**, *123*, 246–250.
[7] A. Boehm, M. Boehm, A. Kogelbauer, *Chem. Ing. Tech.* **2014**, *86*, 883–890.
[8] F. Oeters, M. Ottow, D. Senk, A. Beyzavi, J. Güntner, H. B. Lüngen, M. Koltermann, A. Buhr, in *Ullmann's Encycl. Ind. Chem.* Wiley-VCH Verlag GmbH & Co. KGaA, Weinheim, Germany, **2011**.
[9] H. B. Lüngen, J. Yagi, in *Ullmann's Encycl. Ind. Chem*. Wiley-VCH Verlag GmbH & Co. KGaA, Weinheim, Germany, **2011**.
[10] G. Baldauf-Sommerbauer, S. Lux, M. Siebenhofer, *Green Chem.* **2016**, *18*, 6255–6265.
[11] S. Lux, G. Baldauf-Sommerbauer, M. Siebenhofer, *ChemSusChem* **2018**, https://doi.org/10.1002/cssc.201801356.
[12] C. A. Salotti, A. A. Giardini, *Eos, Trans. Am. Geophys. Union* **1968**, *49*, 342.
[13] A. A. Giardini, C. A. Salotti, *Am. Mineral.* **1969**, *54*, 1151–1172.
[14] R. Emmenegger, *Thermochemische Reaktivität von 3d-Übergangsmetallcarbonaten*, Universität Zürich, **1992**.
[15] A. Reller, R. Emmenegger, C. Padeste, H.-R. Oswald, *Chim. Int. J. Chem.* **1991**, *45*, 262–266.
[16] G. Baldauf-Sommerbauer, S. Lux, J. Wagner, M. Siebenhofer, *Thermochim. Acta* **2017**, *649*, https://doi.org/10.1016/j.tca.2017.01.001.
[17] R. V. Lenth, *Technometrics* **1989**, *31*, 469–473.
[18] Z. Frontistis, E. Hapeshi, D. Fatta-Kassinos, D. Mantzavinos, *Photochem. Photobiol. Sci.* **2015**, *14*, 528–35.
[19] D. C. Montgomery, Design and Analysis of Experiments, **n.d**.
[20] G. Baldauf-Sommerbauer, S. Lux, W. Aniser, B. Bitschnau, I. Letofsky-Papst, M. Siebenhofer, *J. CO2 Util.* **2018**, *23*, 1–9.
[21] G. Baldauf-Sommerbauer, S. Lux, W. Aniser, M. Siebenhofer, *Chem. Eng. Technol.* **2016**, *39*, 2035–2041.
[22] S. S. J. Warne, J. V. Dubrawski, *Thermochim. Acta* **1987**, *121*, 39–49.
[23] G. Baldauf-Sommerbauer, S. Lux, W. Aniser, M. Siebenhofer, *Chem. Ing. Tech.* **2017**, *89*, 172–179.

Received: November 13, 2018